Mon. Not. R. Astron. Soc. **000**, 1–19 (2005) Printed 16 August 2007 (MN LATEX style file v2.2)

Dust in spiral galaxies: global properties

J. A. Stevens,[1⋆] M. Amure[2] and W. K. Gear[2]
[1] *UK Astronomy Technology Centre, Royal Observatory, Blackford Hill, Edinburgh, EH9 3HJ*
[2] *Department of Physics and Astronomy, Cardiff University, PO Box 913, Cardiff CF2 3YB1*

16 August 2007

ABSTRACT

We present and analyse high-quality SCUBA 850- and 450-μm images of 14 local spiral galaxies, including the detection of dust well out into the extended disk in many cases. We use these data in conjunction with published far-infrared flux densities from *IRAS* and *ISO*, and millimetre-wave measurements from ground-based facilities to deduce the global properties of the dust in these galaxies; in particular temperature and mass. We find that simple two-temperature greybody models of fixed dust emissivity index $\beta = 2$ and with typical temperatures of $25 < T_{\rm warm} < 40$ K and $10 < T_{\rm cold} < 20$ K provide good fits to the overall spectral energy distributions. The dust mass in the cold component correlates with the mass in atomic hydrogen and the mass in the warm component correlates with the mass in molecular hydrogen. These results thus fit the simple picture in which the cold dust is heated predominantly by the interstellar radiation field while the hot dust is heated predominantly by OB stars in more active regions, although we argue that there is some mixing. The mean gas-to-dust mass ratio is 120 ± 60, very similar to that found within our own galaxy and roughly a factor of 10 lower than that derived from *IRAS* data alone. The gas-to-dust mass ratios in the warm, molecular component are on average higher than those in the cold, atomic component. We compare our modelling results with similar results for more luminous spiral galaxies selected at far-infrared wavelengths by the SCUBA Local Universe Galaxy Survey and find that whilst the total dust mass distributions of the two samples are indistinguishable, they have significantly different dust temperature distributions in both the warm and cold components. We suggest that this difference might be related to the level of star-formation activity in these systems, with the more active galaxies having more intense interstellar radiation fields and higher dust temperatures.

Key words: galaxies: spiral - galaxies: ISM - submillimetre.

1 INTRODUCTION

The interstellar media (ISM) of galaxies are both the archaeological record of metal production during the star-formation history of the galaxy and the reservoir from which current star-formation draws its material. Despite the great interest in tracing the star formation history and evolution of galaxies surprisingly little is known about the largest sink for metals in the ISM, namely dust grains (see e.g. Whittet 1992; Edmunds 2001).

After the *IRAS* all-sky survey many studies were published of the dust properties in both 'active' and 'normal' galaxies. An influential study was conducted by Devereux & Young (1990; henceforth DY90) in which they derived dust masses from *IRAS* observations of a sample of 58 spiral galaxies and by comparison with CO (as a tracer of H_2) and H I measurements of the gas concluded that the average derived total gas-to-dust mass ratio was $\simeq$1100, compared to the value $\simeq$100 generally found in our own galaxy. DY90 and others recognized that this almost certainly indicated that *IRAS* measurements at 60 to 100 μm were simply not sensitive to the cool dust that may dominate the total dust mass of a galaxy.

Following the launch of *ISO* and the commissioning of SCUBA on the JCMT and MAMBO on the IRAM 30-m telescope, longer wavelength measurements of dust in spiral galaxies have become possible and unsurprisingly several detailed studies have confirmed that indeed there is more dust in spiral galaxies than *IRAS* data alone would suggest (Guélin et al. 1993; Braine et al. 1995, 1997; Neininger & Dumke 1999; Neininger et al. 1996; Dumke et al. 1997; Alton et al. 1998; Haas et al. 1998; Davies et al. 1999; Contursi et al 2001; Popescu et al. 2002; Hippelein et al. 2003; Meijerink et al. 2004). The SCUBA Local Universe Galaxy Survey (SLUGS; Dunne et al. 2000; Dunne & Eales 2001) made brief observations of a large sample of *IRAS*-selected galaxies. They concluded that two dust temperature components were required to fit the spectra, both with an emissivity index $\beta \simeq 2$. In an overlapping study, James et al. (2002) used SCUBA observations of galaxies with known metallicity and the assumption that a constant fraction of metals in a galaxy are bound up in dust grains to derive an absolute dust emissivity consistent with the an extrapolation of the

⋆ E-mail: jas@roe.ac.uk

far-infrared results of Hildebrand (1983) and Casey (1991) with $\beta \simeq 2$.

We have also previously published a study of the dust in NGC 3079 (Stevens & Gear 2000). This paper is a follow-up with a much larger sample. For reasons of brevity we do not in this paper attempt a very detailed study of the morphology of each individual galaxy, which the quality of the images certainly merit, but rather concentrate on the more global properties of the sample and defer more detailed comparison with e.g. CO and H I images to a future paper.

2 SAMPLE

The galaxies observed in no sense constitute a complete or well-defined sample. They were chosen on the basis of being (a) large enough for SCUBA to resolve the core, disc, spiral arm and bar (if present) regions but (b) small enough that it was feasible to chop off the disc (c) bright enough at far-infrared wavelengths to allow mapping with SCUBA with reasonable integration times (of order a few hours) and (d) with published H I and CO measurements. Only spiral galaxies were chosen to enable a comparison of gas and dust content with the Milky Way. Finally, they had to be observable during the time slots awarded, or have data available in the archive. The final sample of 14 sources is given in Table 1. The 850-μm data for NGC 5907 have been published by Alton et al. (2004).

3 OBSERVATIONS AND DATA REDUCTION

The Galaxies marked 'Author' were observed by the authors over the period February 1998 to January 2001. Those marked 'Archive' were observed by others over roughly the same period and the data obtained from the JCMT archive and reduced by the authors.

All observations were obtained using SCUBA in 'jiggle-map' mode with a 120 arcsec chop throw; chop position angle are listed in Table 1. In jiggle-mode the array is shifted sequentially through 64 positions offset by ~ 3 arcsec in order to fully-sample the sky at both 450 and 850 μm. One second is spent in each position, and the telescope is 'nodded' every 16 positions. In many cases, and particularly for the more edge-on sources, several jiggle-maps slightly offset from each other were taken and then combined together, weighted by the rms noise in each individual map, to produce the final image. Skydips were used to monitor the atmospheric emission and flux calibration was performed against Mars, Uranus, CRL 618 and CRL 2688 with at least one and usually two of these sources being observed on each night that data were taken. The flux-conversion factors (FCF) derived from these calibrations were all in good agreement with standard values published on the SCUBA website. We estimate the total uncertainty in the flux densities to be approximately 25 per cent at 450 and 20 per cent at 850 μm respectively, dominated by the uncertainty in determining the atmospheric transmission correction. The SCUBA filters are very narrow, making colour-correction unnecessary.

Data were reduced with the standard STARLINK SURF package (Jenness et al. 2002) with the addition of (1) a custom designed frame-by-frame baseline removal algorithm and (2) modified versions of the SETBOLWT and REBIN tasks. Since these additions were written by ourselves we elaborate on them below.

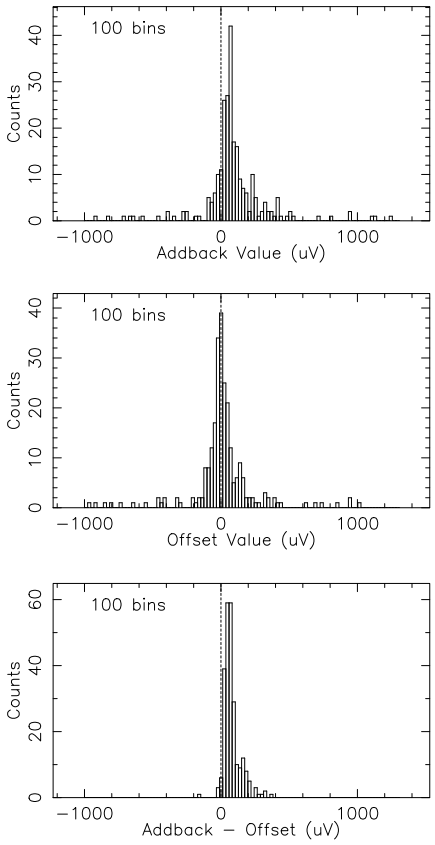

Figure 1. The distribution of 'addback' values that were first removed and then added back onto the data by the SURF task REMSKY (*top*). The distribution of baseline offsets on the individual re-gridded images measured using the STARLINK graphical analysis tool GAIA (*middle*). The difference between the addback value and baseline offset for each image (*bottom*). The units are 10^{-6} Volts.

3.1 Sky removal

The first two steps in the reduction correct for the beamswitching and atmospheric extinction. However, some residual varying sky emission always remains, this emission is strongly correlated between pixels across the array and can be decreased by subtracting the median signal measured in one or several source-free or 'sky' pixels from all the others. Unfortunately, because the galaxies are so extended, it was not possible in many cases to find genuine 'sky' pixels, however since the source flux is also extended and faint it is not strongly detected above the sky in any 1-second jiggle point and so the median value of *all* pixels in the array provides a good measure of the sky emission to be subtracted.

It was found that in some cases the sky emission was clearly not averaging to zero, and hence there was a danger of adding or subtracting spurious flux density from the image. To cure this problem, carefully-selected regions devoid of source emission were identified on the images and defined to be zero to remove the underlying sky emission baseline. It was easier to identify such emission-free regions in the final map than to identify 'sky' bolometers because the jiggling action and sky rotation during an observation means that each bolometer actually moves over a significantly larger area of the source. The regions chosen were also double-checked against other wavelength images from various archives and

Table 1. Parameters of the spiral galaxies in this study

(1) Source	(2) Distance (Mpc)	(3) D_{25} (arcmin)	(4) D_{25} (kpc)	(5) Type	(6) Chop PA (°)	(7) Data source	(8) Environment
NGC 157	35.0	4.27	43.4	SAB(rs)bc	90	Archive	Field
NGC 660	19.6	9.12	52.0	SB(s)a pec	80	Archive	Field
NGC 1808	17.1[a]	7.24	36.0	SAB(s)a	43	Archive	Field
NGC 2903	9.3	12.59	34.2	SAB(rs)bc	90	Author	Field
NGC 3310	21.3	3.63	22.4	SAB(r)bc pec	90	Archive	Field
NGC 3368	15.5	7.08	31.8	SAB(rs)ab	90	Author	Group
NGC 3628	6.7	14.79	28.8	Sb sp pec	14	Archive	Triplet
NGC 4303	20.0	6.03	35.1	SAB(rs)bc	90	Author	Virgo
NGC 4388	20.0	5.13	29.8	SA(s)b sp	0	Archive	Virgo
NGC 4402	20.0	4.07	23.7	Sb sp	0	Author	Virgo
NGC 4414	14.4	3.63	15.2	SA(rs)c	65	Archive	Field
NGC 4501	20.0	6.92	40.3	SA(rs)b	50	Author	Virgo
NGC 4631	12.8	15.14	56.2	SB(s)d sp	0	Author	Pair
NGC 5907	15.6	12.30	55.8	SA(s)c sp	65	Archive	Group

(1) Source name. (2) Distance to the galaxy calculated from the Hubble Law after applying a solar motion correction and using $H_0 = 50$ km s^{-1}Mpc^{-1} (Young et al. 1995). Virgo cluster members are assumed to be at a distance of 20 Mpc. [a]The distance estimate of NGC 1808 is taken from Sofue (1996) using $H_0 = 50$ km s^{-1}Mpc^{-1}. (3) Optical angular diameter out to the 25$^{\rm th}$ mag arcsec^{-2} isophote from de Vaucouleurs, de Vaucouleurs & Corwin (1976). (4) Linear diameter calculated from columns (2) and (3). (5) Morphological type from de Vaucouleurs et al. (1976). (6) Chop position angle measured east of north in the RA-Dec co-ordinate frame. (7) Details of whether the galaxy was observed by the Author or taken from the SCUBA archive. (8) Environment in which the galaxy resides.

confirmed as being unlikely to have significant underlying emission.

The distribution of addback values, of non-zero integrated sky emission baseline-offsets and their 'differences' are shown in Fig. 1. A total of 124 maps were reduced at both 850 and 450 μm giving a total of 248 values.

Since the addback value is the average of the sum of the source flux density seen in the median bolometer value and the sky emission for each data point, the difference is the source flux density seen. This is roughly constant due to the source selection process, i.e. large galaxies which fill the SCUBA field with surface brightness large enough to be detected in a few hours. Almost all values are reassuringly positive, the four negative examples are from noisy maps. The positive tail is due to the relatively brighter galaxy cores. Further discussion of various methods of sky-noise removal and problems associated with them can be found in Amure (2003).

3.2 Regridding

After sky removal each observation was calibrated with the appropriate FCF and the data were processed with the SURF task DESPIKE which sigma-clips after regridding onto sky coordinates. We then used adapted versions of the tasks SETBOLWT and REBIN to weight and regrid the data onto an RA/Dec coordinate frame. The tweaked SETBOLWT task was first used to calculate the standard deviation of the data in each bolometer for the whole dataset to be regridded. We adapted the 'median' option in REBIN so that it uses these standard deviations to calculate a weighted mean and weighted noise map. For some of the galaxies several jiggle-maps were added together, after determining a 'baseline' value for each map from the mean of six 'source-free' regions, setting these all equal to zero, then averaging pixel values in the overlap regions weighted by the inverse-square of the mean noise level in the 'source-free' regions in each individual map. The maps were made with 2-arcsec pixels and then convolved with a Gaussian to improve the signal-to-noise (S/N). We found that a 3-arcsec Gaussian increased the S/N sufficiently on all 850-μm maps to produce a 3-σ detection across most of each galaxy without degrading the resolution significantly. The final resolution of these maps is ~ 15 arcsec. The high-quality 450-μm maps were smoothed with a 2 arcsec Gaussian giving resolutions of ~ 8 arcsec. However, several 450-μm maps had to be smoothed with 4 arcsec Gaussians giving resolutions of ~ 9 arcsec – these galaxies are NGC 3310, NGC 3368, NGC 4303, NGC 4402, NGC 4501 and NGC 5907.

This procedure provides a number of advantages over the default SURF. Primarily, since we have a noise map, we know the S/N at each position on the image and do not have to correct statistically for correlated noise when estimating noise levels from smoothed signal maps (see Dunne & Eales 2001). We can then, for example, plot meaningful S/N contours on the signal maps rather than applying noise estimates calculated from signal-free regions of the signal image to regions where the noise is different.

4 RESULTS

4.1 Submillimetre images

We present the submillimetre images in Figs 2–15. Two types of contour are shown on each image. The white contour is taken from the S/N map and overlaid on the signal map to allow the reader to assess the reality of any faint, extended structure. Note that this procedure is necessary because the noise often varies substantially across SCUBA maps (particularly at 450 μm) because of varying integration time from position to position and changing weather conditions. The black contours, showing levels of equal flux density, are chosen to highlight the extended source structure, any prominent spiral arms and/or bars and the galactic cores. The maps are calibrated into Jy beam^{-1} and are corrected for contamination

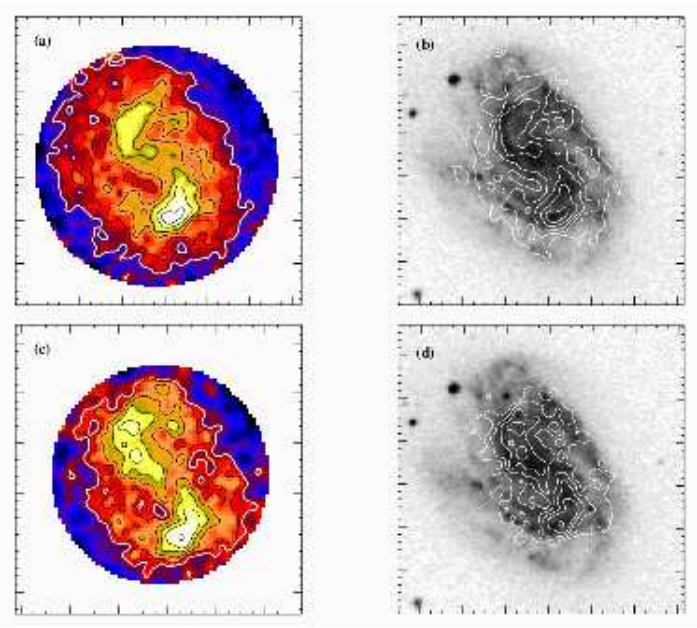

Figure 2. Images of NGC 157 (a) 850-μm image as contoured colour scale. The white contour is the 3-σ level from the signal-to-noise image. Black contours show flux densities of 15, 21, 27, 36 and 45 mJy beam^{-1}. (b) DSS image overlaid with the 850-μm contours. (c) 450-μm image as contoured colour scale. The white contour is the 3-σ level from the signal-to-noise image. Black contours show flux densities of 60, 80, 100, 120 and 160 mJy beam^{-1}. Panels (a) and (b) are 195 arcsec square while panels (c) and (d) are 170 arcsec square.

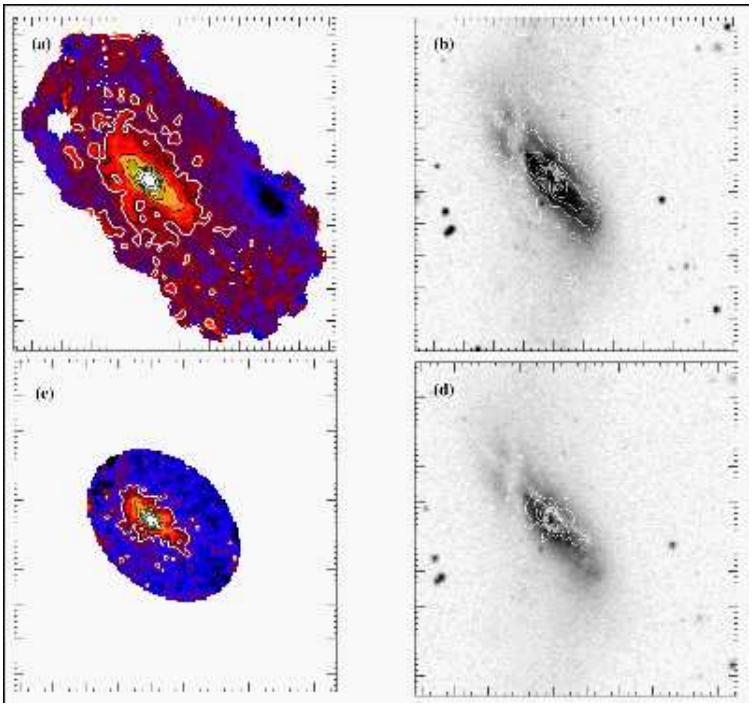

Figure 3. Images of NGC 660 (a) 850-μm image as contoured colour scale. The white contour is the 3-σ level from the signal-to-noise image. Black contours show flux densities of 20, 50, 80, 110, 140, 170, 200 and 230 mJy beam^{-1}. (b) DSS image overlaid with the 850-μm contours. (c) 450-μm image as contoured colour scale – the outer, noisy regions of the image have been trimmed. The white contour is the 3-σ level from the signal-to-noise image. Black contours show flux densities of 260, 440, 620, 800, 970, 1230 and 1500 mJy beam^{-1}. Panels (a) and (b) are 310 arcsec square while panels (c) and (d) are 285 arcsec square.

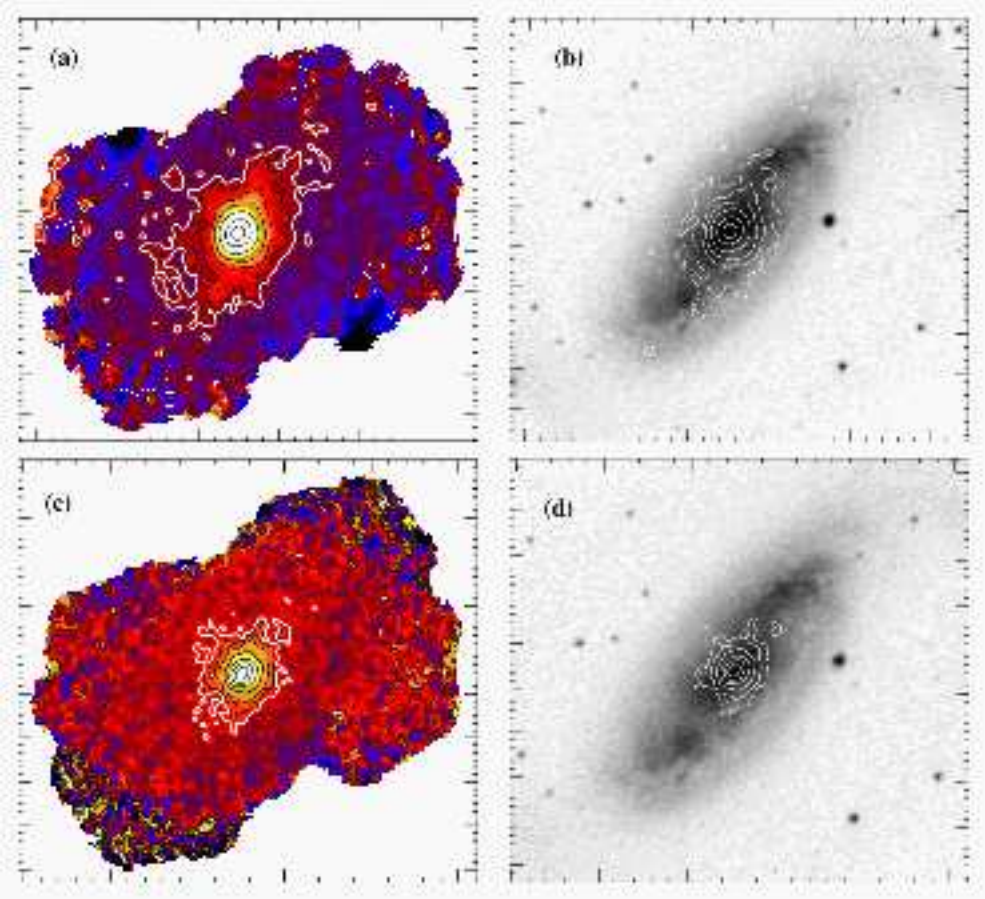

Figure 4. Images of NGC 1808 (a) 850-μm image as contoured colour scale. The white contour is the 3-σ level from the signal-to-noise image. Black contours show flux densities of 15, 30, 50, 100, 200 and 300 mJy beam^{-1}. (b) DSS image overlaid with the 850-μm contours. (c) 450-μm image as contoured colour scale. The white contour is the 3-σ level from the signal-to-noise image. Black contours show flux densities of 150, 250, 450, 700, 1000 and 1300 mJy beam^{-1}. Panels (a) and (b) are 335×310 arcsec while panels (c) and (d) are 310×285 arcsec square.

due to the error beam. These contours are overlaid on both the submillimetre maps and Digitized Sky Survey (DSS) images. The DSS images presented here are from the blue-band second generation survey available from the Space Telescope Science Institute and have a resolution of 1 arcsec.

4.1.1 Comments on individual objects

NGC 157
A prominent thick spiral structure is seen in both the submillimetre maps for this partially inclined galaxy (i = 49°). A high contrast between the arm and inter-arm regions is seen. The peaks of the submillimetre maps are centred on (or very near to) dark lanes within the grand spiral arms of the optical image.

NGC 660
This inclined galaxy (i = 66°) is core dominated in both the submillimetre optical maps. The submillimetre peak is offset from the optical peak by $\sim$ 7 arcsec to the north-west, corresponding to a projected linear offset of $\sim$ 670 pc. However, the intrinsic centre of the distribution of stars (and therefore starlight) in the galaxy is likely to be given by the submillimetre peak. The apparent optical peak may simply be the brightest part of the galactic core that is not obscured by dust.

NGC 1808
The submillimetre maps of this partially inclined galaxy ($i = 60°$) are very core dominated. However, the contours are seen to be elongated along the major-axis on the higher S/N 850-μm map. There is no evidence of the unusual small bar seen in the optical image, approximately 20° offset from the major axis. Even though the optical image is dominated by the core, the starlight from this region may be heavily attenuated by the highly concentrated dust.

NGC 2903
The bar of this spectacular spiral is clearly seen at both 450 and 850 μm. The $\sim$125 arcsec submillimetre bar corresponds to 5.5 kpc at the assumed distance of NGC 2903. Knots of bright submillimetre emission are seen along the length of the bar as well as along the spiral arms attached to the bar ends. There is a very high submillimetre contrast between the bar/arm regions and the inter-arm

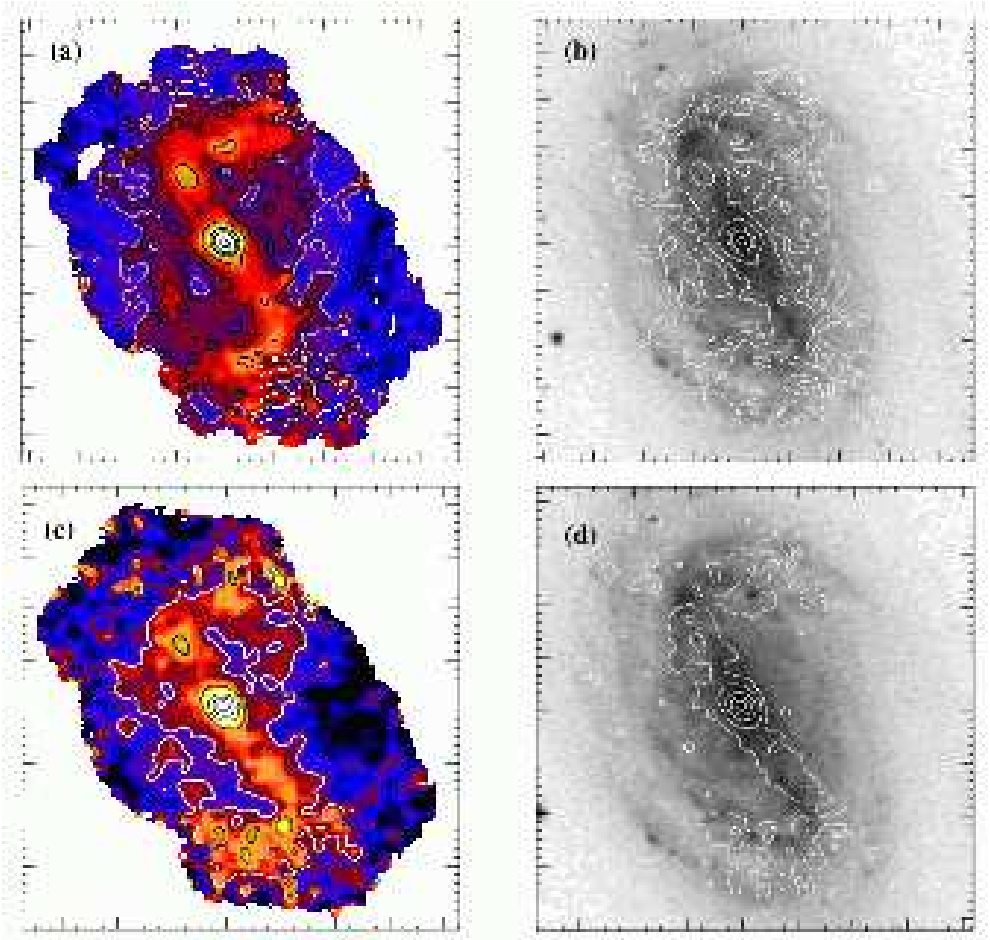

Figure 5. Images of NGC 2903 (a) 850-μm image as contoured colour scale. The white contour is the 3-σ level from the signal-to-noise image. Black contours show flux densities of 15, 25, 50, 75, 100 and 125 mJy beam^{-1}. (b) DSS image overlaid with the 850-μm contours. (c) 450-μm image as contoured colour scale. The white contour is the 3-σ level from the signal-to-noise image. Black contours show flux densities of 80, 150, 250, 350 and 450 mJy beam^{-1}. Panels (a) and (b) are 245×275 arcsec while panels (c) and (d) are 220×255 arcsec.

regions and a bright unresolved galactic core is seen in the submillimetre. There is some danger that we may have chopped some weak extended emission out of this image.

NGC 3310

Submillimetre emission is seen out to $\sim$2/3 of the optical radius in most directions on the 850-μm map. The peak of the submillimetre emission is offset by $\sim$12 arcsec to the north-east from the centre of the optical core. This corresponds to a linear distance of 1.2 kpc at the assumed distance of NGC 3310.

NGC 3368

This mid-inclination galaxy ($i = 45^\circ$) has a least one short bar, which is very well picked out by the submillimetre images. The unresolved core is relatively bright at both submillimetre wavelengths, however the core to bar luminosity ratio appears to be much higher on the 850-μm map, suggesting either the bar contains warm dust or (less likely) the core contains cool dust.

NGC 3628

The optical image of this edge-on galaxy is heavily obscured by a prominent dust lane. The submillimetre emission follows the dust lane extremely well, however it is seen slightly to the north. This effect is caused by the slight inclination of the galaxy on the sky; as the observed submillimetre emission samples both the southern near-side associated with the dust lane, and the unseen northern far side.

NGC 4303

The grand-design spiral arms of this face-on Virgo spiral ($i = 25^\circ$) are mapped at the ends of a north-south running bar in the submillimetre images, especially at 850 μm. As with NGC 2903, bright knots of emission are seen along the bar and arms. There is a strong contrast between the arm and inter-arm regions but the core is still the brightest submillimetre region of NGC 4303. There is some danger that we may have chopped some weak extended emission out of this image.

NGC 4388

Unfortunately this edge-on Virgo spiral ($i = 79^\circ$) was observed under rather poor weather conditions and was not detected at 450 μm. The S/N of the 850-μm is much better; three submillimetre peaks are seen, the central one coincides with the brightest optical region,

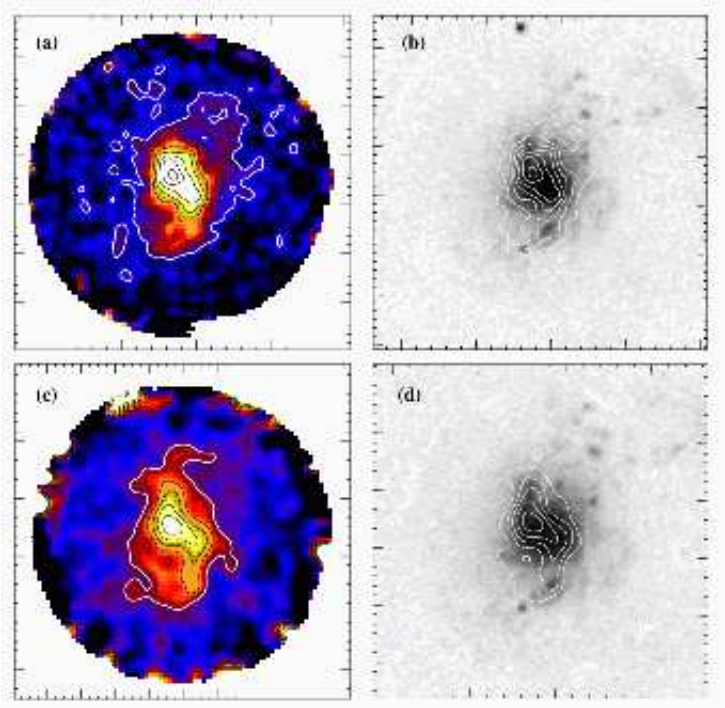

Figure 6. Images of NGC 3310 (a) 850-μm image as contoured colour scale. The white contour is the 3-σ level from the signal-to-noise image. Black contours show flux densities of 6, 11, 16, 21, 26, 31, 36 and 41 mJy beam^{-1}. (b) DSS image overlaid with the 850-μm contours. (c) 450-μm image as contoured colour scale. The white contour is the 3-σ level from the signal-to-noise image. Black contours show flux densities of 40, 60, 80, 100 and 120 mJy beam^{-1}. Panels (a) and (b) are 200 arcsec square while panels (c) and (d) are 170 arcsec square.

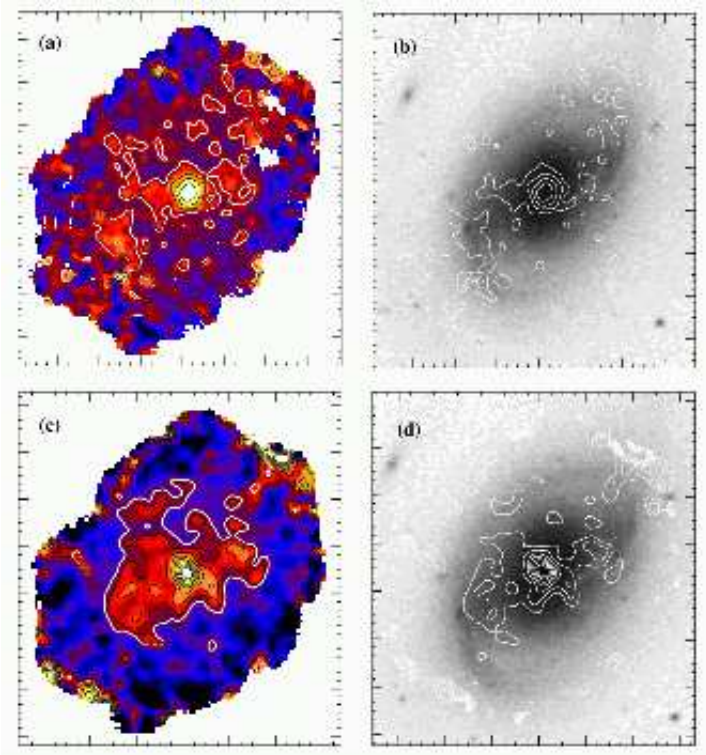

Figure 7. Images of NGC 3368 (a) 850-μm image as contoured colour scale. The white contour is the 3-σ level from the signal-to-noise image. Black contours show flux densities of 15, 30, 50 and 70 mJy beam^{-1}. (b) DSS image overlaid with the 850-μm contours. (c) 450-μm image as contoured colour scale. The white contour is the 3-σ level from the signal-to-noise image. Black contours show flux densities of 80, 110, 140, 170, 200, 230 and 260 mJy beam^{-1}. Panels (a) and (b) are 225 $\times$ 245 arcsec while panels (c) and (d) are 200 $\times$ 220 arcsec.

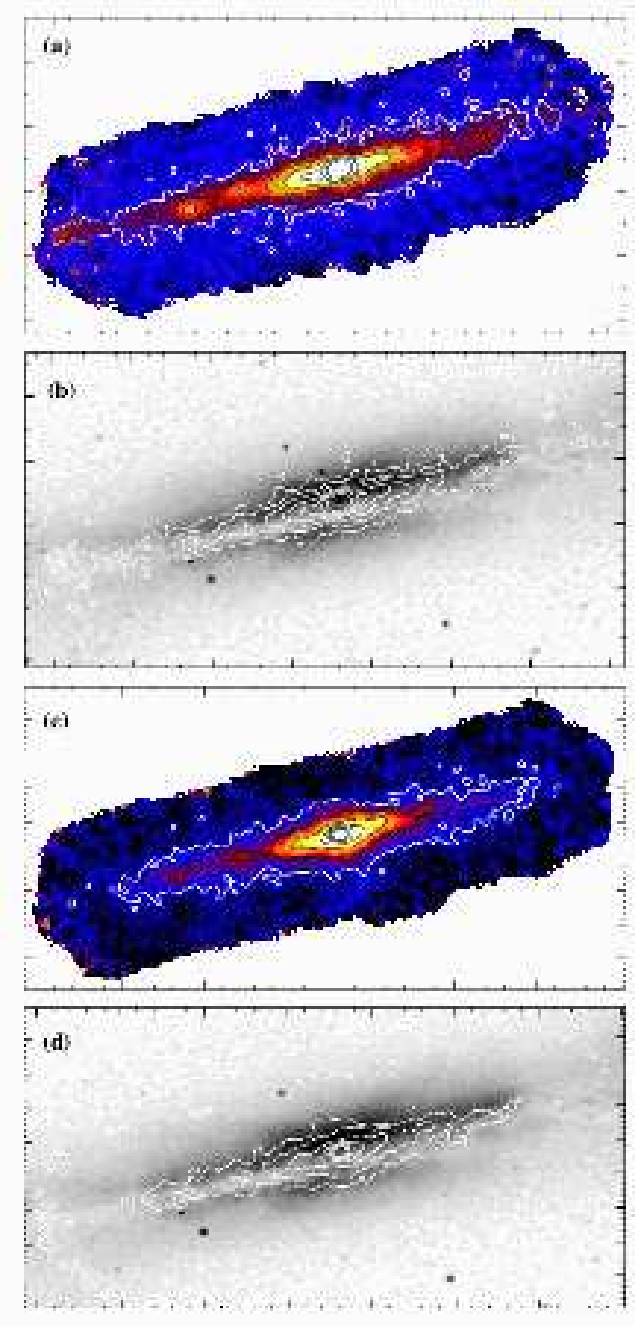

Figure 8. Images of NGC 3628 (a) 850-μm image as contoured colour scale. The white contour is the 3-σ level from the signal-to-noise image. Black contours show flux densities of 15, 30, 50, 80, 110, 140 and 200 mJy beam^{-1}. (b) DSS image overlaid with the 850-μm contours. (c) 450-μm image as contoured colour scale. The white contour is the 3-σ level from the signal-to-noise image. Black contours show flux densities of 100, 200, 400, 600, 800, 1000 and 1200 mJy beam^{-1}. Panels (a) and (b) are 550×290 arcsec while panels (c) and (d) are 525×260 arcsec.

the eastern peak is offset by $\sim$ 28 arcsec and the weaker western peak by $\sim$37 arcsec. These angular distances correspond to 2.7 kpc and 3.5 kpc respectively at the assumed distance to the Virgo cluster. They may be explained as the increased column density seen through a spiral arm on each side of the galactic core. The submillimetre core itself is only slightly brighter than the eastern peak.

NGC 4402

This is a second edge-on Virgo spiral ($i = 75^\circ$), however its optical appearance differs from NGC 4388 as it has a prominent dust lane curving through it. Once again it has three submillimetre peaks, with the central one the brightest, closely followed by the eastern,

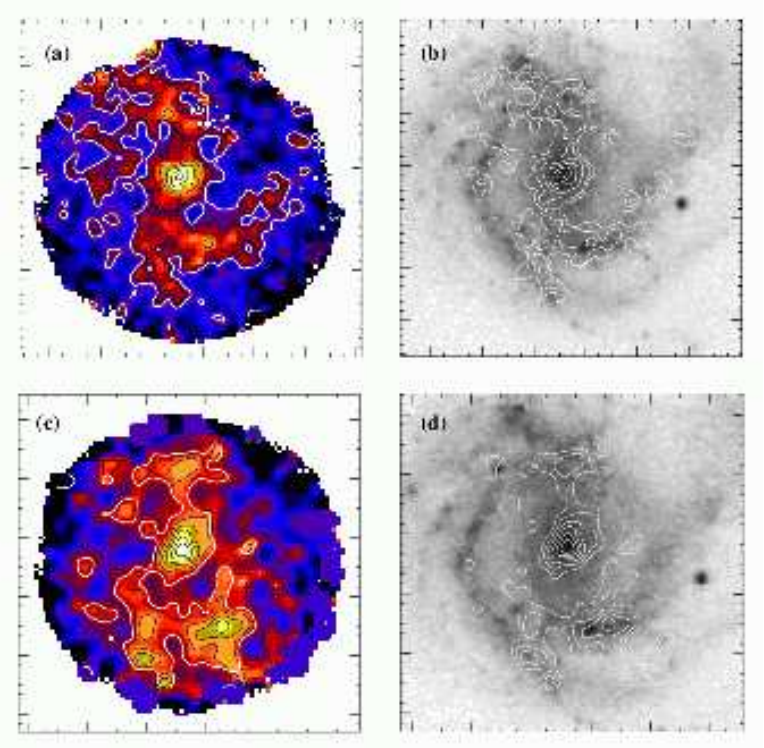

Figure 9. Images of NGC 4303 (a) 850-μm image as contoured colour scale. The white contour is the 3-σ level from the signal-to-noise image. Black contours show flux densities of 18, 24, 36, 48, 60 and 72 mJy beam^{-1}. (b) DSS image overlaid with the 850-μm contours. (c) 450-μm image as contoured colour scale. The white contour is the 3-σ level from the signal-to-noise image. Black contours show flux densities of 70, 90, 110, 130, 150 and 170 mJy beam^{-1}. Panels (a) and (b) are 195 arcsec square while panels (c) and (d) are 170 arcsec square.

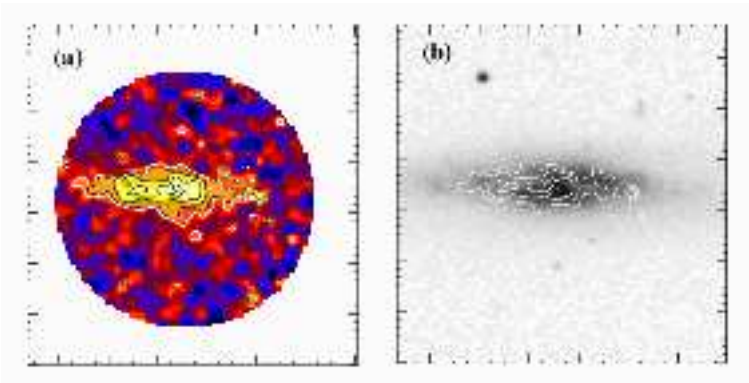

Figure 10. Images of NGC 4388 (a) 850-μm image as contoured colour scale. The white contour is the 3-σ level from the signal-to-noise image. Black contours show flux densities of 20, 30, 40 and 50 mJy beam^{-1}. (b) DSS image overlaid with the 850-μm contours. The panels are 195 arcsec square.

and then finally the western peak which is barely recognizable as above the disc emission.

NGC 4414

This mid-inclination spiral ($i = 54^\circ$) is thought to be in front of the Virgo cluster. It has two central peaks which are best explained as the enhanced line-of-sight column densities seen through a ring orbiting the galactic core. The $\sim$30 arcsec separation of the peaks corresponds to a linear distance of 2.1 kpc at the assumed distance to NGC 4414. The idea of a dusty ring surrounding the core is supplemented by the molecular gas hole detected in the same region by Sakamoto et al. (1999).

NGC 4501

Unfortunately both SCUBA bolometer arrays were so noisy throughout the observations of this mid-inclination Virgo spiral ($i = 58^\circ$) that 25 per cent of the 450-μm bolometers and 40 per cent of the 850-μm bolometers had to be blanked. Nonetheless, submillimetre emission is detected from the galaxy and its peak coincides with the optical centre.

NGC 4631

The submillimetre emission from this large galaxy ($i = 85^\circ$)has been mapped over almost 14 arcmin which corresponds to a linear distance of 52 kpc at the assumed distance to NGC 4631. This is 92 per cent of the optical radius out to the 25$^{\rm th}$ mag isophote. Several features are seen in the submillimetre maps including, three central peaks, a warp in the western side of the disc, knots of bright emis-

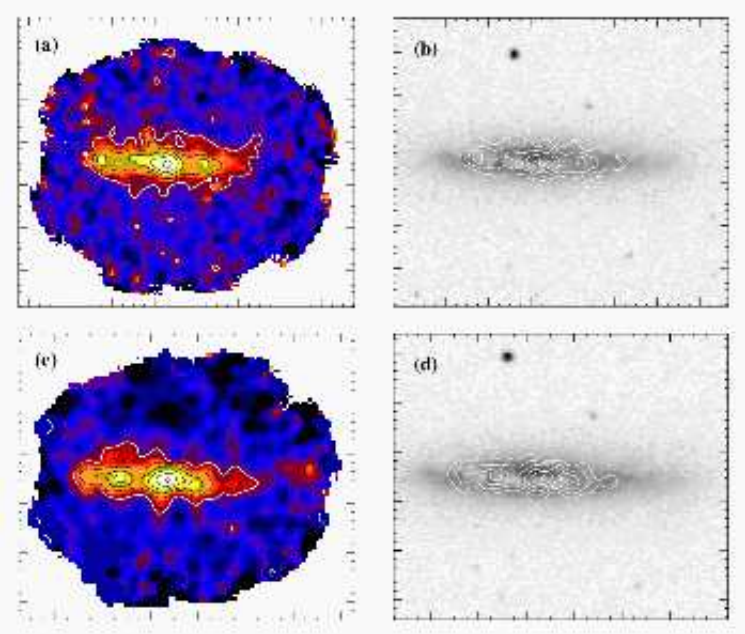

Figure 11. Images of NGC 4402 (a) 850-μm image as contoured colour scale. The white contour is the 3-σ level from the signal-to-noise image. Black contours show flux densities of 15, 25, 35, 45 and 55 mJy beam^{-1}. (b) DSS image overlaid with the 850-μm contours. (c) 450-μm image as contoured colour scale. The white contour is the 3-σ level from the signal-to-noise image. Black contours show flux densities of 70, 100, 130, 160, 190 and 220 mJy beam^{-1}. Panels (a) and (b) are 230 $\times$ 200 arcsec while panels (c) and (d) are 200 $\times$ 170 arcsec.

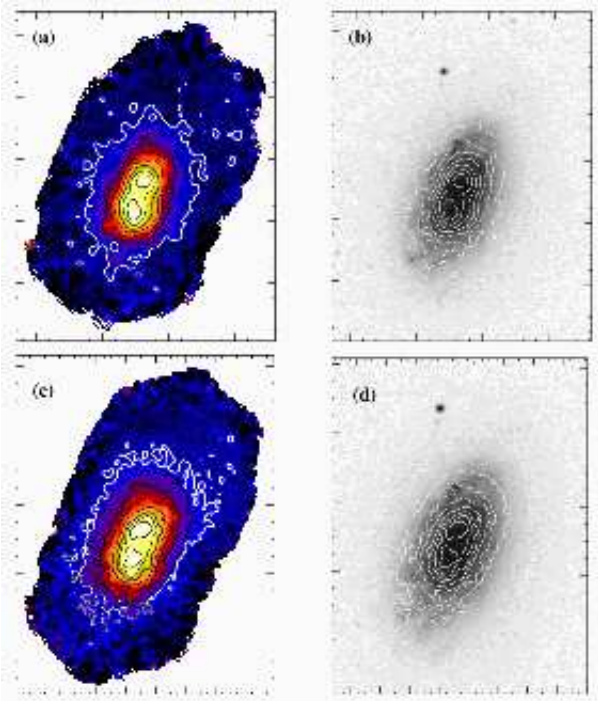

Figure 12. Images of NGC 4414 (a) 850-μm image as contoured colour scale. The white contour is the 3-σ level from the signal-to-noise image. Black contours show flux densities of 10, 20, 30, 40, 50, 60 and 70 mJy beam^{-1}. (b) DSS image overlaid with the 850-μm contours. (c) 450-μm image as contoured colour scale. The white contour is the 3-σ level from the signal-to-noise image. Black contours show flux densities of 40, 80, 120, 160, 200, 240 and 280 mJy beam^{-1}. Panels (a) and (b) are 250 $\times$ 315 arcsec while panels (c) and (d) are 220 $\times$ 310 arcsec.

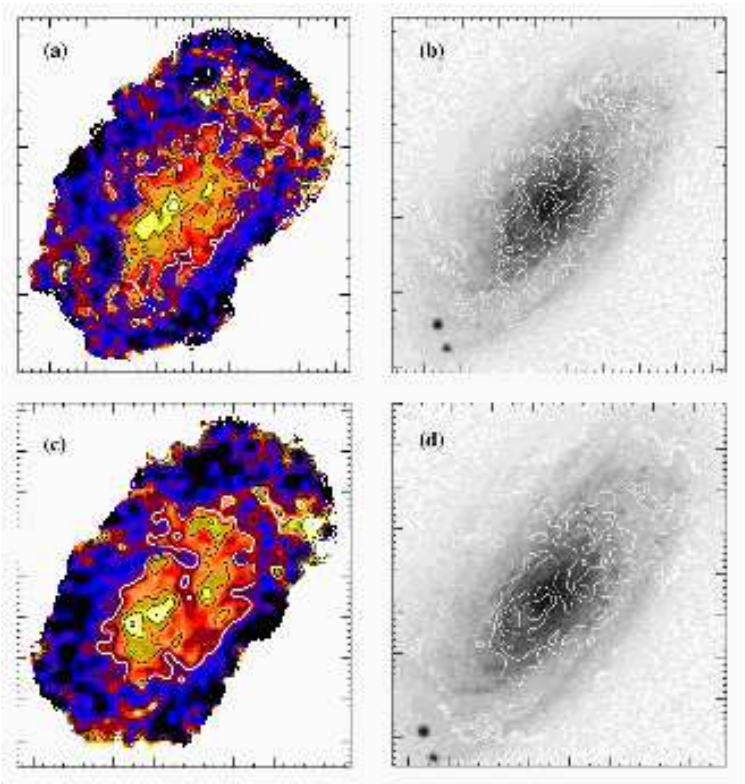

Figure 13. Images of NGC 4501 (a) 850-μm image as contoured colour scale. The white contour is the 3-σ level from the signal-to-noise image. Black contours show flux densities of 15, 25, 35 and 45 mJy beam^{-1}. (b) DSS image overlaid with the 850-μm contours. (c) 450-μm image as contoured colour scale. The white contour is the 3-σ level from the signal-to-noise image. Black contours show flux densities of 80, 120, 160 and 200 mJy beam^{-1}. Panels (a) and (b) are 265×265 arcsec while panels (c) and (d) are 240×260 arcsec.

sion along the disc and filamentary structure emanating like smoke from chimneys away from the plane of the disc.

The three central peaks may be explained from a dusty torus surrounding the centre of the galaxy, as seen in the edge-on galaxies NGC 4388 and NGC 4402. The ~ 80 arcsec separation of the two outer peaks correspond to a diameter of 4.9 kpc at the assumed distance to NGC 4631. The eastern peak is brighter than the western one, however in this case both are brighter than the central peak. The 850-μm emission, and arguably the 450-μm emission, is seen to peak twice more ~ 90 arcsec either side of the central peak, corresponding to a linear distance of 5.5 kpc. These peaks may be due to the increased line of sight column densities through two main spiral arms.

NGC 5907

The galaxy is almost perfectly edge-on ($i = 89°$). The majority of the submillimetre emission is extremely well confined to a thin disc and is well mapped out to just over half the optical radius. It is seen to be dominated by the core which is unresolved by SCUBA in the direction perpendicular to the galactic plane. A few bright knots of submillimetre emission are seen along the disc. The two peaks ~ 75 arcsec either side of the centre correspond to a linear distance of 5.7 kpc at the assumed distance to the galaxy. A third, more distant northern peak seen on the 850-μm map is 120 arcsec from the centre, or 9.1 kpc. All three may be due to the increased dust column density along the line of sight through spiral arm regions within the galactic disc.

4.2 Flux densities

We present total submillimetre flux densities in Table 2. For each galaxy we made signal-to-noise maps and determined the 1-σ contour level. This contour could be approximated by an elliptical aperture. Flux densities were calculated by summing the emission in these apertures placed on the signal maps, and uncertainties by adding in quadrature the data in the corresponding aperture placed on the noise map. Calibration uncertainties were calculated from the variation in the sky opacity and variation of FCF across the night when the data was taken.

Some of the galaxies have low surface brightness emission extending across the whole map. We estimated this additional emission for each galaxy by repeating the above procedure and simply summing the total emission on the map. Using this method, we find that five galaxies have higher flux densities at one or both wavelengths. In addition, if the optical radius of the galaxy exceed our 2 arminute chop throw there is a danger of missing very extended flux. However this is a danger only for NGC 2903 and NGC 4303, both of which appear to have their emission strongly dominated by their prominent bars.

Global 60- and 100-μm *IRAS* flux densities were taken from the literature. The primary source was data presented for the *IRAS* Bright Galaxy Sample by Soifer et al. (1989), although 4 objects have flux densities taken from other publications. These far-infrared flux densities, all used in subsequent modelling, are listed in Table 2 along with references to their literature sources. We supplemented these values with published data at 1300 μm for

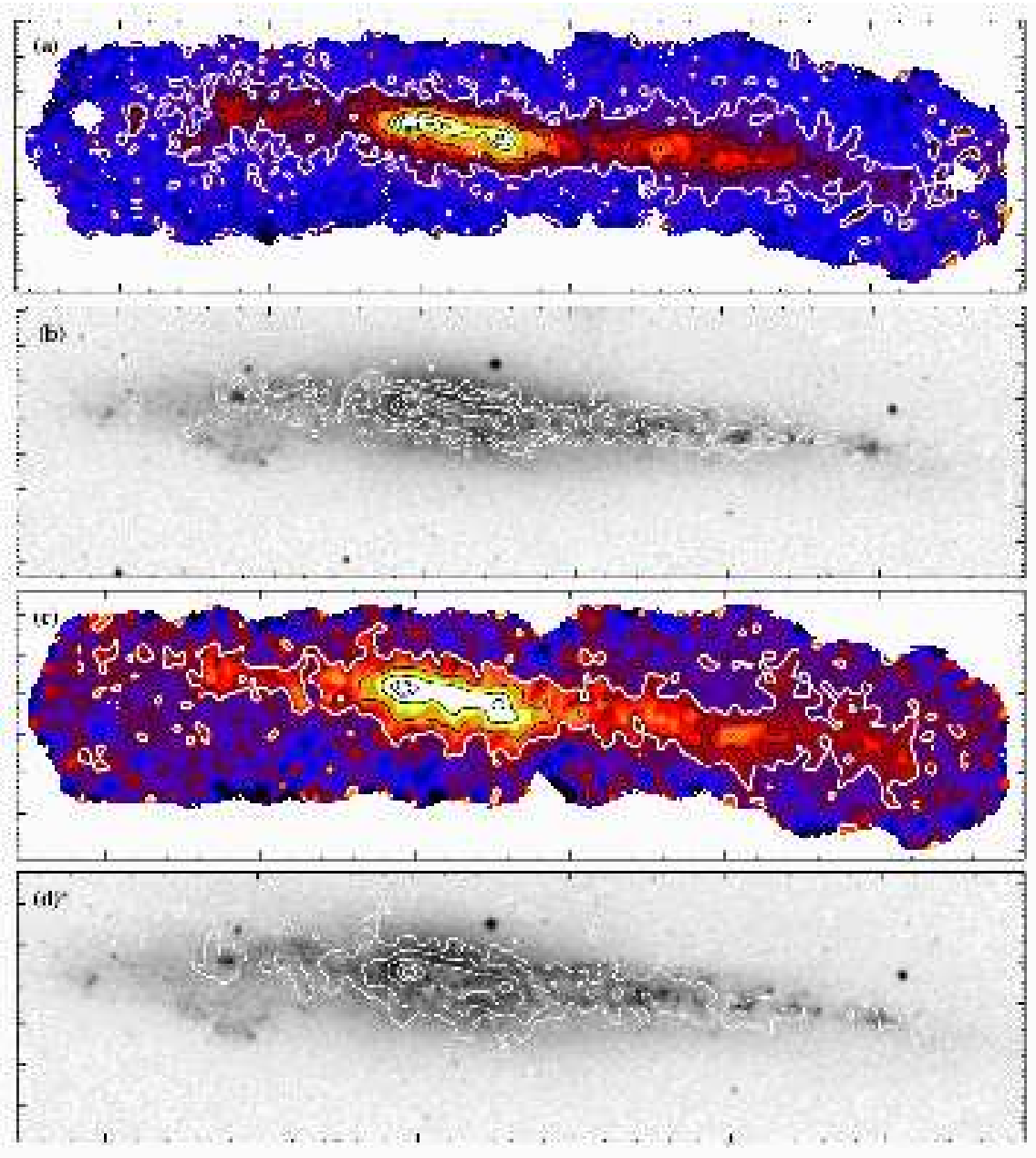

Figure 14. Images of NGC 4631 (a) 850-μm image as contoured colour scale. The white contour is the 3-σ level from the signal-to-noise image. Black contours show flux densities of 20, 30, 45, 80, 100 and 120 mJy beam^{-1}. (b) DSS image overlaid with the 850-μm contours. (c) 450-μm image as contoured colour scale. The white contour is the 3-σ level from the signal-to-noise image. Black contours show flux densities of 50, 100, 200, 300 and 350 mJy beam^{-1}. Panels (a) and (b) are 845 $\times$ 225 arcsec while panels (c) and (d) are 820 $\times$ 200 arcsec.

NGC 660 (Chini et al. 1986); at 170 μm for NGC 4388 and NGC 4402 (Tuffs et al. 2002); at 180 μm (Bendo et al. 2003), 870 and 1230 μm (Dumke, Krause & Wielebinski 2004) for NGC 4631; and at 1200 μm (Dumke et al. 1997) for NGC 5907. We also include our previously published data for NGC 3079 (Stevens & Gear 2000) together with the revised ISOPHOT data presented by Klaas & Walker (2002), and include this galaxy in subsequent analysis. For NGC 5907, Alton et al. (2004) report a total flux density of 1.6 Jy ($\pm$15 per cent) at 850 μm which is consistent with our value within the quoted uncertainties.

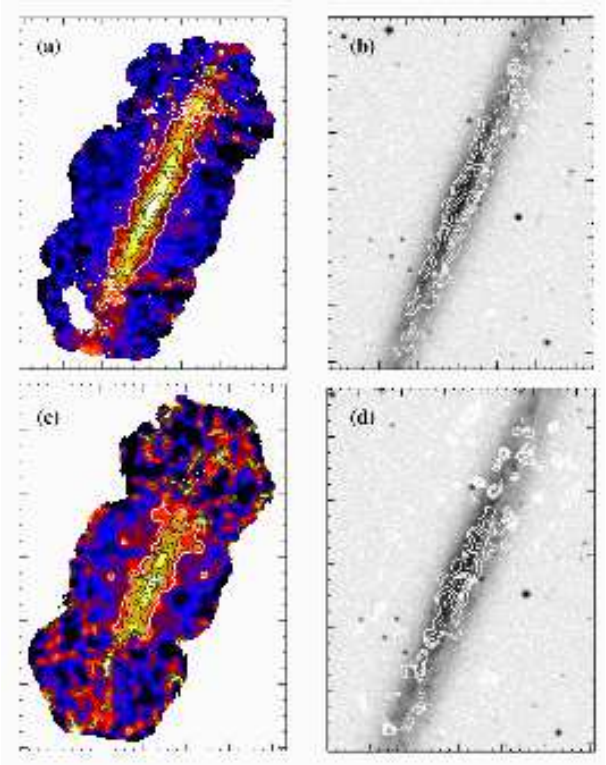

Figure 15. Images of NGC 5907 (a) 850-μm image as contoured colour scale. The white contour is the 3-σ level from the signal-to-noise image. Black contours show flux densities of 15, 20, 25, 30 and 35 mJy beam^{-1}. (b) DSS image overlaid with the 850-μm contours. (c) 450-μm image as contoured colour scale. The white contour is the 3-σ level from the signal-to-noise image. Black contours show flux densities of 150, 200, 250, 300 and 350 mJy beam^{-1}. Panels (a) and (b) are 280×370 arcsec while panels (c) and (d) are 250×345 arcsec.

Table 2. Submillimetre (this work) and far-infrared (*IRAS*) flux densities.

(1)	(2)	(3)	(4)	(5)	(6)	(7)
	Flux density to 1σ contour		Flux density in map		*IRAS* far-infrared flux densities	
Source	S_{850} (mJy)	S_{450} (mJy)	S_{850} (mJy)	S_{450} (mJy)	S_{100} (Jy)	S_{60} (Jy)
NGC 157	910 ± 13	4734 ± 81	…	…	43.1 ± 4.3^a	17.6 ± 1.8^a
NGC 660	1360 ± 12	6925 ± 186	1393 ± 20	8832 ± 662	104.9 ± 10.5^b	67.3 ± 6.7^b
NGC 1808	1301 ± 22	7138 ± 135	…	8133 ± 271	137.2 ± 5.5^c	87.8 ± 3.5^c
NGC 2903	1796 ± 26	7936 ± 232	…	…	147.4 ± 22.1^b	52.4 ± 7.9^b
NGC 3310	358 ± 8	1293 ± 52	…	1406 ± 71	48.0 ± 4.8^a	34.1 ± 3.4^a
NGC 3368	513 ± 23	3439 ± 120	…	…	30.4 ± 3.0^a	10.7 ± 1.1^a
NGC 3628	2822 ± 184	16934 ± 196	…	…	106.0 ± 10.6^a	51.6 ± 5.2^a
NGC 4303	705 ± 20	4602 ± 172	…	…	79.7 ± 8.0^a	37.5 ± 3.8^a
NGC 4388	234 ± 13	…	294 ± 21	…	17.4 ± 1.7^a	10.1 ± 1.0^a
NGC 4402	357 ± 10	2309 ± 94	445 ± 21	2772 ± 169	17.5 ± 1.8^a	5.4 ± 0.5^a
NGC 4414	1160 ± 12	7543 ± 60	…	…	69.1 ± 6.9^a	30.1 ± 3.0^a
NGC 4501	962 ± 27	6386 ± 186	…	…	63.7 ± 6.4^a	17.6 ± 1.8^a
NGC 4631	5253 ± 46	25056 ± 1731	…	…	170.4 ± 34.1^d	90.7 ± 18.2^d
NGC 5907	1962 ± 33	13188 ± 908	…	…	45.8 ± 6.9^b	8.8 ± 1.3^b

(1) Source name. (2) and (3) 850- and 450-μm flux density calculated by summing the emission to the 1-σ contour (see text for more details). (4) and (5) Total 850- and 450-μm flux density in the map if different from that within the 1-σ contour. The quoted uncertainties represent the noise in the given aperture placed on the noise maps. The total error is dominated by the calibration uncertainty which we estimate to be ~ 20 per cent at 850 μm and ~ 25 per cent at 450 μm (see text). (6) and (7) 100 and 60 μm flux density from *IRAS*. These values are used in the model fits. Literature sources are: *a* – Soifer et al. (1989); *b* – Rice et al. (1988); *c* – Moshir et al. (1990); *d* – Young et al. (1989).

4.3 Model fitting the spectral energy distributions

In this section we fit simple models to the spectral energy distributions (SEDs) to estimate the temperatures and masses of the dust components in our spiral galaxies. Although, the dust is likely to be radiating at a range of temperatures, simple two component models are often chosen to describe the far-infrared–millimetre SEDs of galaxies. The choice is partly motivated by physical considerations and partly demanded by lack of the data required to constrain more complex models. Physically one might identify the warm component with dust heated predominantly by OB stars and the cold component with dust in 'cirrus' clouds heated by the interstellar radiation field (ISRF).

We choose to fit the data with two optically thin greybody functions, giving an equation of the form,

$$S(\lambda) = N_{\rm w} B(\lambda, T_{\rm w}) Q_{\rm em}(\lambda) + N_{\rm c} B(\lambda, T_{\rm c}) Q_{\rm em}(\lambda) \quad (1)$$

where S is the flux density at wavelength λ, $N_{\rm w}$ and $N_{\rm c}$ are the normalizations, $B(\lambda, T)$ is the Planck function, $T_{\rm w}$ and $T_{\rm c}$ are the warm and cold dust temperatures and $Q_{\rm em}$ is the wavelength-dependent emissivity of the grains which varies as $\lambda^{-\beta}$ over the wavelength range considered. We further assume that β has a fixed value of 2 which is the typical value found for galaxies (see e.g. the discussion in Dunne & Eales 2001). We thus have four free parameters; the two normalizations and the two temperatures.

Five of the galaxies have enough data points to constrain this model by minimizing χ^2. These fits are presented in Table 3 and Fig. 17. In Fig. 17 the confidence limits for the fitted temperatures can be estimated roughly by the reader by projecting the χ^2 contours onto the axes. Note that these estimates give the confidence limits for our adopted model and are not absolute. The reduced χ^2 values and probabilities show that all fits are acceptable (values of $Q > 0.001$ are often assumed to indicate adequate fits to real data). For the remaining ten galaxies, which all have four data points, the fits are formally unconstrained; we simply give the minimum χ^2 in Table 3 and show these fits in Fig. 18. Inspection of Table 3 shows that constrained and unconstrained fits return temperatures and normalization ratios with similar ranges. We thus use the full sample in subsequent analysis.

First, we calculate the dust mass of each component in the standard manner using,

$$M_{\rm d} = S(\lambda) D^2 / [k_{\rm d}(\lambda) B(\lambda, T)] \quad (2)$$

where D is the distance to the galaxy and $k_{\rm d}$ is the mass absorption coefficient for which we assume a value 0.077 m^2 kg^{-1} at 850 μm (Draine & Lee 1984). Note that the ratio of the fitted normalizations gives the ratio of the masses in the warm and cold dust components. We then calculate the ratio of luminosity in the cold component to that in the warm by integrating under the fitted curves. The 'far-infrared' luminosity ($L_{\rm FIR}$) is calculated similarly by summing the luminosity in both components. All of these quantities are given in Table 3.

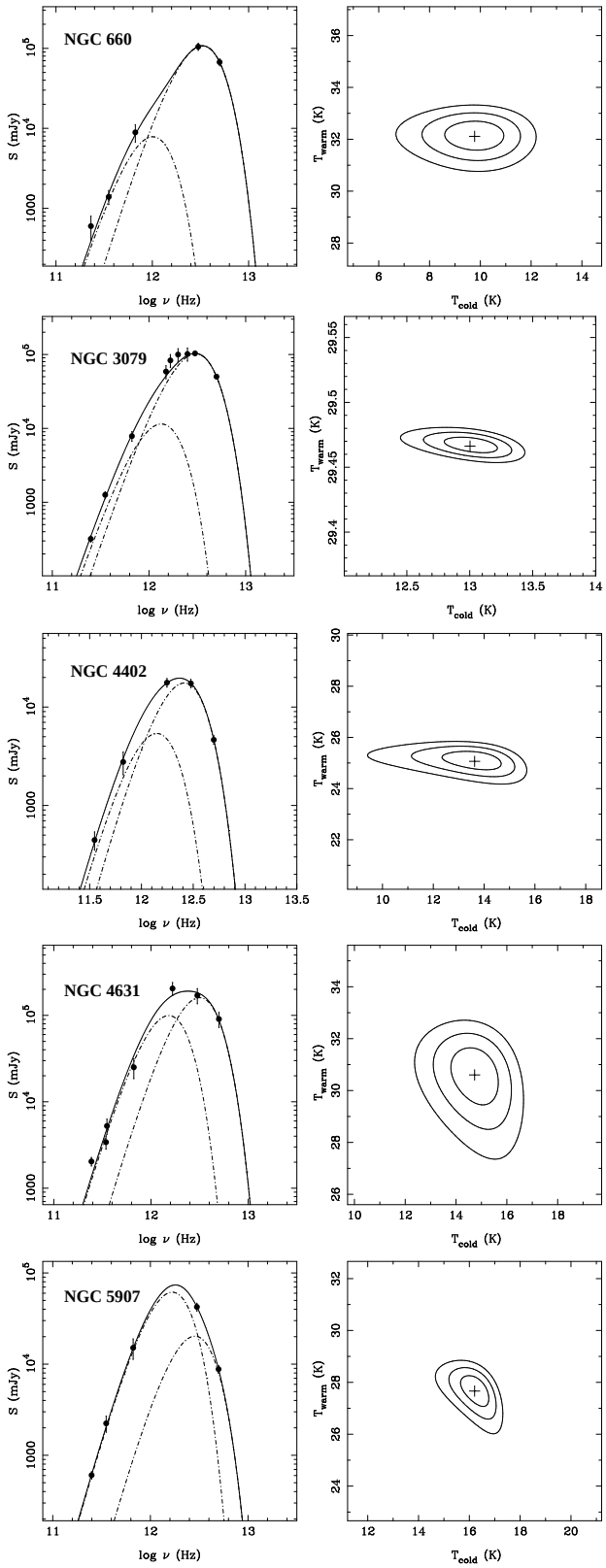

Figure 17. Model fits for those galaxies with more than 4 data points. On the left-hand panels the dot-dashed lines show the warm and cold component optically-thin greybody fits with a fixed emissivity index, $\beta = 2$. The solid line is the sum of these two components. The right-hand panels show contours of χ^2 at 1-, 2- and 3-σ confidence intervals for the fitted temperatures calculated while keeping the fitted normalizations fixed. The cross on each right-hand panel marks the position of minimum χ^2.

5 DISCUSSION

5.1 Gas and dust

All of our galaxies have been mapped in the CO(1-0) line, a tracer of molecular hydrogen, and the 21 cm line of atomic hydrogen. The gas masses computed from these data are now used together with the dust masses from the model fits to search for correlations

Table 3. Model fitting results.

(1) Source	(2) T_w (K)	(3) T_c (K)	(4) N_c/N_w	(5) M_d (Log $M_\odot$)	(6) L_c/L_w	(7) L_{FIR} (Log $L_\odot$)	(8) χ^2/ν	(9) Q
NGC 660	32	10	28	8.34	0.02	10.69	1.5	0.23
NGC 3079	29	13	7	8.11	0.06	10.84	1.0	0.40
NGC 4402	25	13	6	7.55	0.14	9.88	0.2	0.70
NGC 4631	38	17	99	8.12	0.75	10.62	5.3	1.2×10^{-3}
NGC 5907	28	16	48	7.94	1.76	10.15	0.2	0.66
NGC 157	28	9	22	8.67	0.03	10.75	...	...
NGC 1808	32	11	13	8.03	0.02	10.70	...	...
NGC 2903	28	5	46	8.35	< 0.01	10.11	...	...
NGC 3310	33	8	300	9.04	0.06	10.47	...	...
NGC 3368	27	12	8	7.48	0.06	9.89	...	...
NGC 3628	29	10	37	7.72	0.05	9.74	...	...
NGC 4303	29	9	9	7.97	0.01	10.55	...	...
NGC 4388	31	14	17	7.37	0.18	9.86	...	...
NGC 4414	29	12	11	7.78	0.06	10.20	...	...
NGC 4501	25	10	5	8.00	0.21	10.41	...	...

(1) Source name. (2) Cold dust temperature. (3) Warm dust temperature. (4) Ratio of cold-to-warm dust. (5) Total dust mass. (6) Ratio of luminosity in the cold component with luminosity in the hot component. Luminosities are calculated by integrating under the fitted curves. (7) Far-infrared luminosity calculated by integrating under both fitted curves. (8) Minimum reduced χ^2. (9) Q gives the probability that the observed reduced chi-square will exceed the value χ^2 by chance even for a correct model. The first five rows show results for galaxy spectra with more than 4 data points whereas the remainder have only 4 data points and the fits are unconstrained.

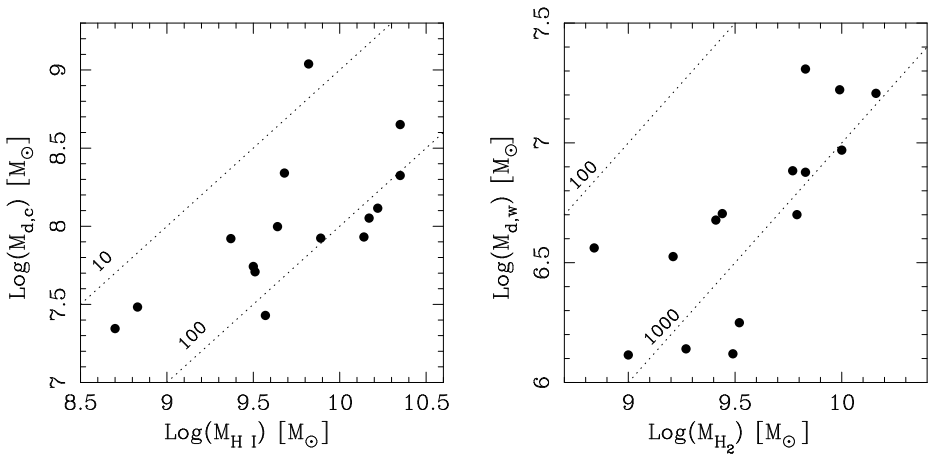

Figure 16. Correlations between (left) mass of atomic hydrogen and mass of dust in the cold component, and (right) mass of molecular hydrogen and mass of dust in the warm component . Both correlations are significant at the > 3-σ level (see text). The dotted lines on each panel are gas-to-dust mass ratios of the indicated level.

between these quantities, and to quantify the gas-to-dust mass ratios. Global CO(1-0) fluxes were taken from the Five Colleges Radio Astronomy Observatory Extragalactic CO Survey (Young et al. 1995) and converted to molecular gas masses (M_{H_2}) using a conversion factor $X_{CO} = 2.8\times10^{20}$ H_2 mol cm^{-2} (K km s^{-1})$^{-1}$. Atomic hydrogen masses (M_{H_I}) were taken from the literature. These quantities are given in Table 4 along with references to the literature sources. Also given are ratios between the H I mass and cold dust mass ($M_{d,c}$), the H_2 mass and warm dust mass ($M_{d,w}$) and the total gas-to-dust mass ratio (M_g/M_d) where $M_g = M_{H_2} + M_{H_I}$.

In Section 4.3 we raised the idea that the cold dust might trace the atomic hydrogen and the warm dust the molecular hydrogen. The dust masses of these components derived from our model fits are compared with the relevant gas mass in Fig. 16. A Spearman rank-order test returns a correlation coefficient, $r = 0.78$ and probability that the correlation is real, $P > 0.999$ for the former case and $r = 0.79$, $P > 0.999$ for the latter. Both correlations are significant at > 3-σ confidence. However, no correlation is found between either cold dust mass and molecular hydrogen mass ($r = 0.21$, $P = 0.55$) or between warm dust mass and atomic hydrogen mass ($r = 0.26$, $P = 0.66$). These results lend weight to our assertion and show that the model fits are returning physically meaningful quantities. An obvious next step would be to investigate the spatial correspondence between dust and gas emission, and to search for variations in submillimetre spectral index as a function of position within the galaxies. However, since such detailed decompositions

Table 4. Gas masses from the literature, calculated gas-to-dust mass ratios and star-formation efficiencies.

(1) Source	(2) $M_{\rm H_I}$ (Log $M_\odot$)	(3) $M_{\rm H_2}$ (Log $M_\odot$)	(4) $M_{\rm H_I}/M_{\rm d,c}$	(5) $M_{\rm H_2}/M_{\rm d,w}$	(6) $M_{\rm g}/M_{\rm d}$	(7) $L_{\rm w}/M_{\rm H_2}$ ($L_\odot\,M_\odot^{-1}$)	(8) $L_{\rm FIR}/M_{\rm g}$ ($L_\odot\,M_\odot^{-1}$)
NGC 157	10.35[a]	9.83	50	332	63	8.1	1.9
NGC 660	10.09[b]	10.08	106	896	110	7.1	1.7
NGC 1808	9.64[c]	(i) 9.77	44	769	95	8.3	4.9
NGC 2903	9.68[d]	9.41	22	539	33	5.0	1.8
NGC 3079	10.17	10.16	131	898	229	4.5	2.4
NGC 3310	9.82[e]	8.84	6	190	7	40.2	4.0
NGC 3368	9.57[f]	9.21	138	483	174	4.5	1.5
NGC 3628	9.51	(ii) 9.27	63	1348	98	2.8	1.1
NGC 4303	9.89[g]	10.00	92	1072	191	3.5	2.0
NGC 4388	8.70[g]	9.00	23	768	65	6.1	4.8
NGC 4402	8.83[h]	9.44	22	543	98	2.4	2.2
NGC 4414	9.50[i]	9.79	57	1228	155	2.4	1.7
NGC 4501	9.37[g]	9.99	28	586	120	2.2	2.1
NGC 4631	10.22[j]	9.49	127	2344	148	7.7	2.1
NGC 5907	10.14[k]	9.52	162	1863	195	3.6	0.8
		Mean	71 ± 49	924 ± 562	119 ± 61	7.2 ± 9.1	2.3 ± 1.2

(1) Source name. (2) Mass of atomic hydrogen. (3) Mass of molecular hydrogen. (4) ratio between masses in atomic hydrogen and cold dust. (5) ratio between masses in molecular hydrogen and warm dust (6) Total gas-to-dust mass ratio. (7) star-formation efficiency calculated from the luminosity in the warm component and the mass in molecular hydrogen. (8) global star-formation efficiency. References: a – Ryder et al. (1998); b – van Driel et al. (1995); c – Dahlem, Ehle & Ryder (2001); d – Wevers, van der Kruit & Allen (1986); e – Mulder, van Driel & Braine (1995); f – Devereux & Young (1990; reference within to Warmels 1986); g – Cayatte et al. (1990); h – Giovanelli & Haynes (1983); i – Braine, Combes & van Driel (1993); j – Rand (1994); k – Dumke et al. (1997; reference within to Huchtmeier & Richter 1989); All H_2 masses are from Young et al. (1995) *except* (i) Mass taken from Haynes, Giovanelli & Roberts (1979; scaled for distance). (ii) Mass taken from Dahlem et al. (1990; scaled for distance and $X_{\rm CO}$).

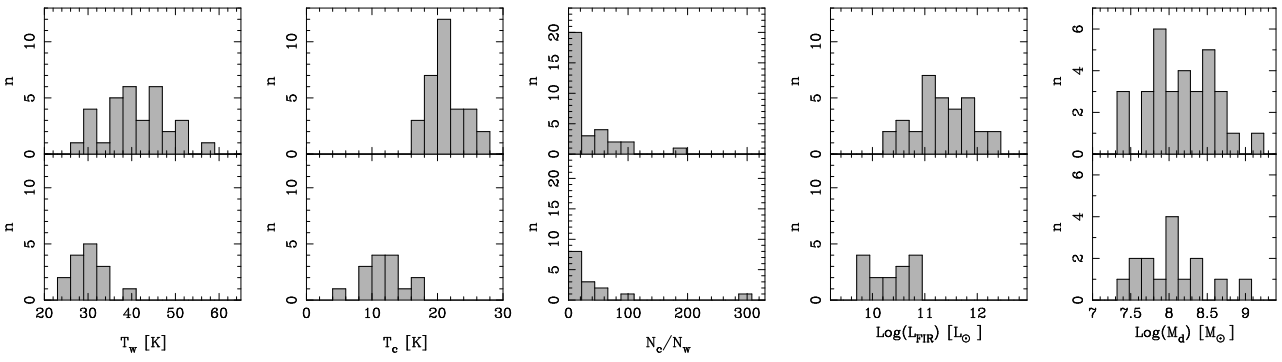

Figure 19. Histograms of quantities derived from the model fits showing (from left to right) the distributions of warm temperature, cold temperature, ratio of mass in the cold to mass in the warm component, logarithm of far-infrared luminosity and logarithm of the dust mass. The top panels show data from the SLUGS survey (Dunne & Eales 2001) while the bottom panels show data from this work.

do not readily fit the scope of this work we defer them to a future paper.

The mean total gas-to-dust mass ratio of 119 ± 61 is a factor ~ 10 below the mean value derived by DY90 (1080 ± 70) from *IRAS* data alone and entirely equivalent to the mean value within our own galaxy. For the latter, Sodroski et al (1997) report gas-to-dust mass ratios of $\sim 70 - 270$ for the H I component and $\sim 140 - 400$ for the H_2 component, both showing a systematic decline towards the Galactic centre (we have applied a correction factor to take account of the different mass absorption coefficient used in that study compared to ours). These ratios are consistent with the mean values from this study given in Table 4. The fact that in a sample of similar spiral galaxies to our own we obtain a very similar global ratio suggests we have now identified essentially all of the dust in these sources.

Although the scatter is large, there is evidence that the gas-to-dust mass ratios in the warm (molecular) components are systematically higher than those in the cold (atomic) components (Table 4 and Fig. 16). This result is, however, contrary to that expected since the gas-to-dust mass ratio in galaxies is known to de-

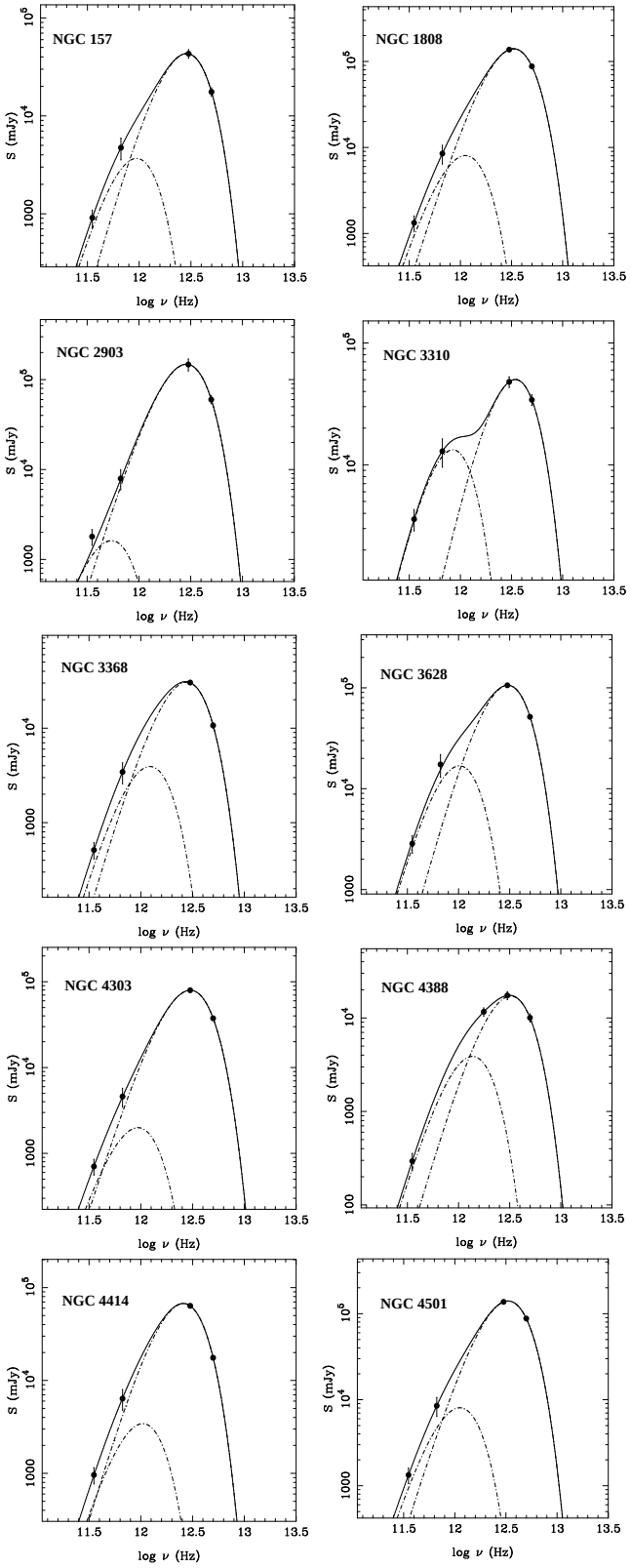

Figure 18. Minimum χ^2 fits for those galaxies with only 4 data points. The dot-dashed lines show the warm and cold component optically thin greybody fits with a fixed emissivity index, $\beta = 2$. The solid line is the sum of these two components.

crease with increasing metallicity (e.g. Whittet 1992). One possibility might be that $X_{\rm CO}$ varies as a function of environment. In fact, for NGC 3079, Braine et al. (1997) calculate a value for the core region that is roughly one order of magnitude below that derived for the disk. However, they also find that the molecular gas mass of NGC 3079 is dominated by the disk component so while this effect does not lead to an order of magnitude reduction in the gas-to-dust mass ratio, it would reduce it to some extent, and possibly by a more substantial amount in other galaxies. On the other hand, the gas-to-dust mass ratios might be raised in these active regions if dust grain mantles are destroyed while the CO molecules are left intact.

It has been argued that a good measure of the activity of a galaxy is its star-formation efficiency which is simply the efficiency of converting mass into luminosity, and is defined as $L_{\rm FIR}/M_{\rm g}$ (e.g. Chini et al. 1986). Very active star-forming galaxies are found to have $L_{\rm FIR}/M_{\rm g} \sim 100\ {\rm L}_\odot\,{\rm M}_\odot^{-1}$ while quiescent systems such as spiral galaxies have $L_{\rm FIR}/M_{\rm g} \sim 5\ {\rm L}_\odot\,{\rm M}_\odot^{-1}$ (Chini et al. 1995). In Table 4 we list the star-formation efficiencies for our spiral galaxies; we give both the global measure and the measure for the warm molecular component. As expected the star-formation efficiencies are higher for the latter but in only one case (NGC 3310) do they approach the typical value found for active systems. While this could be taken as evidence that these galaxies do not contain regions of substantial active star-formation there is inevitably some degree of 'smearing' when measuring the global properties of these systems. A more detailed comparison of the dust emission and molecular gas emission is required. For example, Braine et al. (1997) used millimetre wavelength dust continuum and CO observations of similar spatial resolution to those presented here to show that the central region of NGC 3079 has $L_{\rm FIR}/M_{\rm g} \sim 100\ {\rm L}_\odot\,{\rm M}_\odot^{-1}$ whereas the disk has $L_{\rm FIR}/M_{\rm g} \sim 6-7\ {\rm L}_\odot\,{\rm M}_\odot^{-1}$.

5.2 Dust masses, temperatures and luminosities

It is instructive to compare the model fitted parameters from Section 4.3 with those determined for other galaxies, including our own Milky Way. We first consider results for SLUGS galaxies which were selected from the *IRAS* Bright Galaxy Sample (Dunne & Eales 2001). The models used in this paper are identical to those fitted to the SLUGS galaxies, and we have used the same dust parameters (mass absorption coefficient). The two samples, once corrected for different assumed cosmologies, are thus directly comparable. We plot histograms of selected quantities from Table 3 in Fig. 19. It is apparent that our heterogeneously-selected sample has a lower mean far-infrared luminosity $\{{\rm Log}[\overline{L}_{\rm FIR}\ ({\rm L}_\odot)] = 10.3 \pm 0.4\}$ than the SLUGS sample $\{{\rm Log}[\overline{L}_{\rm FIR}\ ({\rm L}_\odot)] = 11.0 \pm 0.5\}$. This difference also appears to hold for the distributions of warm dust temperature ($\overline{T}_{\rm w} = 30 \pm 3$ K cf. $\overline{T}_{\rm w} = 41 \pm 7$ K for SLUGS) and cold dust temperature ($\overline{T}_{\rm c} = 11 \pm 3$ K cf. $\overline{T}_{\rm c} = 21 \pm 3$ K for SLUGS). The far-infrared-selected galaxies have on average higher dust temperatures for both components. The distributions of normalization ratio and dust mass, however, look similar. These results are confirmed with the application of two-sample Kolmogorov-Smirnov (K-S) tests (Table 5).

What is the physical origin of this difference in dust temperature? The equilibrium temperature of a dust grain is a function of both the grain properties and the energy density in the ISRF. While it is possible that the properties of the dust grains differ in the warm and cold components the fact that the lower luminosity galaxies have lower dust temperatures argues for a connection between

Table 5. K-S test results.

(1) Samples	(2) KS	(3) probability
$T_{\rm w}$	0.75	> 0.999
$T_{\rm c}$	0.97	1.00
$N_{\rm c}/N_{\rm w}$	0.18	0.16
$L_{\rm FIR}$	0.78	> 0.999
$M_{\rm d}$	0.26	0.59

(1) Test samples. (2) K-S statistic. (3) Probability that datasets are drawn from different distributions.

star-formation activity and dust temperature. Global star-formation efficiencies can be calculated for 14 of the SLUGS galaxies. As expected, they are typically higher than those found for our sample (Table 4) with a range $2-32$ $\rm L_{\odot}\,M_{\odot}^{-1}$ and a mean of 9 ± 9 $\rm L_{\odot}\,M_{\odot}^{-1}$. Since the temperatures of both components appear to vary in concert the nature of the star-formation process must be such that the heating is not confined solely to dust in molecular clouds. Some fraction of energy emitted by OB stars must escape the molecular cores and heat dust in less dense regions. Thus an increase in star-formation activity would have a wider impact than naively expected from the simple two component model.

Finally in this section, we compare our results with those obtained for the Milky Way. The total far-infrared luminosity is 7.4×10^{9} $\rm L_{\odot}$ of which ~ 60 per cent is from dust associated with the H I component (Sodroski et al. 1997). Inspection of the model fits and the $L_{\rm c}/L_{\rm w}$ values from Table 4 shows that only NGC 5907 has this property. The far-infrared luminosity of the other galaxies appears to be dominated by the warmer dust component that we associate predominantly with H_2. Dust temperatures for the Milky way are presented by Reach et al. (1995) who find three characteristic ranges of $16-21$, $10-13$ and $4-7$ K. Thus in the context of our sample of spiral galaxies the Milky Way is less luminous and contains dust radiating at lower temperatures.

5.3 Effect of environment

Because we have a mixture of field and Virgo cluster spirals in our sample we can try to make a comparison of the gas to dust ratios in the different environments. It is well known that some Virgo spirals are deficient in H I, presumably due to stripping, however H_2 is not depleted (Kenney & Young 1986, 1988a,b, 1989; Stark et al. 1986). Leggett, Brand & Mountain (1987) claimed that there was no difference in the *IRAS* emission from field and Virgo spirals, consistent with the idea that *IRAS* traced warm dust associated with well-bound molecular clouds. However, Doyon & Joseph (1989) found evidence that H I deficient galaxies in the Virgo cluster have lower 60- and 100-μm flux densities and cooler far-infrared colour temperatures than those with normal H I content. They conclude that for a typical spiral in the core of the cluster, at least half the diffuse dust has been stripped. If true then then we might expect to see a difference at longer wavelengths. Specifically, if the cold dust that is mixed with the H I is also stripped from the Virgo galaxies then this difference would be reflected in the $N_{\rm c}/N_{\rm w}$ ratios determined in the model fits since these give the mass of dust in the cold component relative to that in the warm component. The values found for the Virgo galaxies are indeed all relatively small (9, 17, 6 and 5) with a mean value of just 9 ± 5. For comparison, the non-Virgo members have a mean value of 56 ± 81 or 31 ± 26 excluding NGC 3310. However, the samples are not formally distinct; a two-sample K-S test returns a KS statistic of 0.64 with a probability of 0.89 (1.6 σ) that the two datasets are drawn from different distributions. Observations of much larger samples would be required to investigate the effect of environment any further.

6 CONCLUSIONS

We have presented high-quality submillimetre images of 14 spiral galaxies. Simple two-component model fits to the global SEDs show that:
(1) The dust is typically radiating at temperatures of $10-20$ K and $25-40$ K and in most cases the warm component dominates the total luminosity.
(2) The dust mass in the warm component correlates with the mass in molecular hydrogen while the dust mass in the cold component correlates with the mass in atomic hydrogen. The opposite correlations are not significant. This result suggests that the simple two-component models provide a good approximation to the real physical nature of these galaxies.
(3) The mean gas-to-dust mass ratio of 120 ± 60 is entirely consistent with that reported for the Milky Way. There is evidence that the ratio is higher in the warm, molecular component.
(4) Comparing our model results with those found for the SLUGS survey, we find that our galaxies have, on average, similar dust masses but lower far-infrared luminosities and lower dust temperatures for both the warm and cold components. We suggest that the lower dust temperatures found for our galaxies can be linked to reduced star-formation activity and thus less intense ISRFs than those present in the SLUGS galaxies.

The next step will be to analyse the emission from the individual galaxies in more detail. In particular to investigate both the correspondence of dust and gas emission and to search for differences in submillimetre spectral index as a function of galactocentric radius.

ACKNOWLEDGMENTS

MA acknowledges the support of a PPARC studentship. We thank Loretta Dunne for insightful comments on the pre-submitted manuscript, Ashley James for helpful discussions on dust properties and the referee for constructive criticism. Guest User, Canadian Astronomy Data Centre, which is operated by the Dominion Astrophysical Observatory for the National Research Council of Canada's Herzberg Institute of Astrophysics. This research has made use of the NASA/IPAC Extragalactic Database (NED) which is operated by the Jet Propulsion Laboratory, California Institute of Technology, under contract with the National Aeronautics and Space Administration. The DSS images presented in this paper were obtained from the Multimission Archive at the Space Telescope Science Institute (MAST). STScI is operated by the Association of Universities for Research in Astronomy, Inc., under NASA contract NAS5-26555. Support for MAST for non-HST data is provided by the NASA Office of Space Science via grant NAG5-7584 and by other grants and contracts.

REFERENCES

Alton P.B., Bianchi S., Rand R.J., Xilouris E., Davies J.I. Trewhella M., 1998, ApJ, 507, L125

Alton P.B., Xilouris E.M., Misiriotos A., Dasyra K.M., Dumke M., 2004, A&A, 425, 109

Amure M., 2003, Ph.D. Thesis, Cardiff University

Bendo G.J., et al. 2003, AJ, 125, 2361

Braine J., Combes F., van Driel W., 1993, A&A, 280, 451

Braine J., Krugel E., Sievers, A., Wielebinski R., 1995, A&A, 344, L1

Braine J., Guélin M., Dumke M., Brouillet N., Herpin F., Wielebinski R., 1997, A&A, 326, 963

Casey S.C., 1991, ApJ, 371, 183

Cayatte V., van Gorkom J.H., Balkowski C., Kotanyi C., 1990, AJ, 100, 604

Chini R., Kreysa E., Krügel E., Mezger P.G., 1986, A&A, 166, L8

Chini R., Krügel E., Lemke R., Ward-Thompson D., 1995, A&A, 295, 317

Contursi A., Boselli A., Gavazzi G., Bertagna E., Tuffs R., Lequeux J., 2001, A&A, 365, 11

Dahlem M., Aalto S., Klein U., Booth R., Mebold U., Wielebinski R., Lesch H., 1990, A&A, 240, 237

Dahlem M., Ehle M., Ryder S.D., 2001, A&A, 373, 485

Davies J.I., Alton P., Trewhella M., Evans R., Bianchi S., 1999, MNRAS, 304, 495

Devereux N.A., Young J.S., 1990, ApJ, 359, 42 (DY90)

de Vaucouleurs G. de Vaucouleurs A. Corwin H., 1976, Second Reference Catalogue of Bright Galaxies, University of Texas Press, Austin

Doyon R., Joseph R.D., 1989, MNRAS, 239, 347

Draine B.T., Lee H. M., 1984, ApJ, 285, 89

Dumke M., Krause M., Wielebinski R., 2004, A&A, 414, 475

Dumke M., Braine J., Krause M., Zylka R., Wielebinski R., Guelin M., 1997, A&A, 325, 124

Dunne L., Eales S., Edmunds M., Ivison R., Alexander P., Clements D.L., 2000, MNRAS, 315 ,115

Dunne L., Eales S. A., 2001, MNRAS, 327, 697

Edmunds M.G., 2001, MNRAS, 328, 223

Giovanelli R., Haynes M.P., 1983, AJ 88, 881.

Guélin M., Zylka R., Mezger P.G., Haslam C.G.T., Kreysa E., Lemke R., Sievers A.W., 1993, A&A, 279, L37.

Haas M., Lemke D., Stickel M., Hippelein H., Kunkel M., Herbstmeier U. Mattila K.. 1998, A&A, 338, L33

Haynes M.P., Giovanelli R., Roberts M.S. 1979, ApJ 229,83.

Hildebrand R.H., 1983, QJRAS, 24, 267

Hippelein H., Haas M., Tuffs R.J., Lemke D., Stickel M., Klaas U., Völk H.J., 2003, A&A, 407, 137

Holland W.S., et al., 1999, MNRAS, 303, 659

Huchtmeier W.K., Richter O.-G, 1989, A general Catalog of H I Observations of Galaxies; The reference Catalog, XIX. Springer-verlag, New York.

James A., Dunne L., Eales S.A., Edmunds M.G., 2002, MNRAS, 335, 753

Jenness T., Stevens J.A., Archibald E., Economou F., Jessop N.E., Robson E.I., 2002, MNRAS, 336, 14

Kenney J.D., Young J., 1986, ApJ, 301, L13

Kenney J.D., Young J., 1988a, ApJ, 326, 588

Kenney J.D., Young J., 1988b, ApJS, 66, 261

Kenney J.D., Young J., 1989, ApJ, 344, 761

Klass U., Walker H. J., 2002, A&A, 391, 911

Leggett S.K., Brand P., Mountain C.M. 1987, MNRAS, 228, L11

Moshir M., et al., 1990, IRAS Faint Source Catalogue, version 2.0

Meijerink R., Tilanus R.P.J., Dullemond C.P., Israel F.P., van der Werf P.P., 2004, A&A, in press (astro-ph/0409511)

Mulder P.S., van Driel W., Braine J., 1995, A&A, 300, 687

Neininger N., Guélin M., Garcia-Burillo S., Zylka R. Wielebinski R., 1996, A&A, 310, 725

Neininger N., Dumke M. 1999, Proc.Nat.Acad.Sci, 96, 5360

Popescu C.C., Tuffs R.J., Völk H.J., Pierini D., Madore B.F., 2002, ApJ, 567, 221

Reach W.T., et al., 1995, 451, 188

Rand R.J., 1994, A&A, 285, 833

Rice W., Lonsdale C.J., Soifer B.T., Neugebauer G., Koplan E.L., Lloyd L.A., de Jong T., Habing H.J., 1988, ApJS, 68, 91

Ryder S.D., Zasov A.V., McIntyre V.J., Walsh W., Sil'chenko O. K., 1998, MNRAS, 293, 411

Sakomoto K., Okumura S.K., Ishizuki S., Scoville N.Z. 1999, ApJS, 124, 403

Sodroski T.J., Odegard N., Arendt R.G., Dwek E., Weiland J.L., Hauser M.G., Kelsall T., 1997, ApJ, 480, 173

Soifer B.T., Boehmer L., Neugebauer G., Sanders D.B., 1989, AJ, 98, 766

Stark A.A., Knapp G.R., Bally J., Wilson R.W., Penzias A.A., Roe H.E., 1986, ApJ, 310 ,660

Stevens J.A., Gear W.K., 2000, MNRAS, 312, L5

Tuffs R.J., et al., 2002, ApJS, 139, 37

van Driel W. et al., 1995, AJ, 109, 942

Warmels R.H., 1986, PhD thesis, University of Groningen

Wevers B.M.H.R., van der Kruit P.C., Allen R.J., 1986, A&AS 66, 505

Whittet D.C.B., 1992, Dust in the Galactic Environment, Institute of Physics (IOP) Publishing, Bristol

Young J.S., Xie S., Kenney J.D.P., Rice W.L., 1989, ApJS, 70, 669

Young J.S. et al., 1995, ApJS, 98, 219

This paper has been typeset from a TEX/ LATEX file prepared by the author.